Link to publication

University of Bath

Alternative formats

If you require this document in an alternative format, please contact:
openaccess@bath.ac.uk

EM-skin: an artificial robotic skin using magnetic inductance tomography

Gavin Dingley, Mackenzie Cox, and Manuchehr Soleimani

Abstract— **Physical sensing by touch is essential for building intelligent artificial systems in robotic manipulation and human-robotic interaction. Inductive skins are being investigated as part of a major effort to develop the most robust and reliable touch sensors, mainly based on traditional proximity sensing. Magnetic induction tomography (MIT) is primarily considered for medical diagnostics and industrial process monitoring, by reliably using magnetic inductances in a coil array. This article presents a novel electromagnetic-based skin (EM-skin) using the principle of MIT imaging, by processing the mutual inductance data from a planar array of sensors. The paper demonstrates multi-touch, dynamical touch, and quantitative touch pressure imaging. MIT data is captured at 10 frames/s, so allowing for dynamical touch analysis. The results show the successful reconstruction of dynamical sensing, where two applied cyclic touch points, with different frequencies are discriminately detected. Quantitively force sensing shows the detection of a 120 mN force, which translates to 0.38 kP of applied pressure in the described system. These results will open the way to a new generation of distributed and reliable soft skins that are versatile due to material design and processing.**

Index Terms— **Magnetic induction tomography, tactile sensing, artificial skin, EM-skin, mutual inductance array**

I. I. INTRODUCTION

CONTACT awareness is an essential part of robotics operation and vital in controlling human-machine interaction (HMI) [1]. Tactile information measured when the robotic skin interacts with the outside world can provide stimulus feedback, allowing machines to interact with their environment. Moreover, soft contact sensing and their resolved forces can be incorporated into other applications, such as gait analysis [2], [3], [4], [5]. These can help detect abnormal movements and model the mechanical behaviors of the HMI. Despite these benefits, the advantages of contact and touch feedback are still underexploited because of difficulties in the realization of cost-effective performances, which include high resolution, good stability, and challenges in scalability for large area touch sensing.

Existing contact-force tactile sensors operate based on either active or passive sensing. The active sensing measures physical parameters that are then translated to a force mapping, using either electrical [7], [9], magnetic [6], optical [8], or acoustic methods [1]. On the passive sensing side, the piezoelectric material has attracted a lot of attention because it does not require a power source to measure contact force [10]. Camera-based tactile sensors are often large and hard to implement on hidden surfaces.

Variation in magnetic fields, induced by contact forces acting on soft materials, which are embedded with either magnets [5] or magnetic powders [6], has also been explored for contact sensing. In this study, we introduce a novel mutual inductance-based sensing employing magnetic induction tomography (MIT). The development of MIT is largely concentrated on medical and industrial applications [11]. MIT uses the measurement of mutual inductances between coils arranged as an array of sensors. In this work, using an image reconstruction method, the mapping of a wide range of force stimuli in multiple-touch soft skin is demonstrated. Tomographic approaches provide an autonomous method of sense area mapping with an increased resolution compared to proximity inductive detectors [13]. Distributed sensing measurement data is obtained using a planar coil array responding to the deformation and displacement of a soft metallic sensing membrane. In our EM-skin, the spatial tactile transduction relies on a soft sensing area made from a metallic or magnetic material. This work demonstrates the EM-skin by verification of static and dynamic touch experiments.

The paper is organized as follows: section II describes the skin sensor, the operation of the MIT device, and the software for image formation. Of particular interest is the use of a measured touch to voltage sensitivity map that enables the reconstruction of forces and touches derived directly from MIT data. Sections III, IV, and V show the experimental verification of the proposed tomographic sensors in multi-touch sensing, dynamical touch responses and force quantifications. Conclusions are drawn in section VI putting the results into the context of future use of such a tomographic-based skin.

II. MATERIALS AND METHODS

In an MIT measurement system, an alternating electrical current flowing in the excitation coil induces voltages in the detector coils, which are recorded. The voltage induced in the detector coil is dependent upon the excitation field frequency and coupling factor, which includes the physical dimensions of the sensing and detecting coils, as well as the passive electromagnetic properties of materials within the field of view of the excitation-detector coil pair.

A.   Measurement system

The MIT devices used in this study involve an 8-channel and a 16-channel system. An overview of the device operation is explained as follows: An AVR 8-bit microcontroller is used in both instruments to configure, control, and provide communication with a host PC. Array field coils are driven using a power operational amplifier, the input sinusoid is generated by a DDS IC (direct digital synthesis), where a programmable gain amplifier (PGA) provides amplitude control. On the receive side of the system, another PGA is used to amplify the detected signal, where a precision rectifier and filter network find the absolute value, captured using a 16-bit ADC. Configuration of the two PGAs mitigates the frequency dependence of coil drive impedance and sensitivity. Sequential scanning of the array is furnished by two multiplexers, one for receive and the other for transmit. The multiplexers are banks of solid-state relays addressed using line decoders. A similar 8-channel system was also used in these investigations. Fig. 1 is a system diagram of the 16-channel system, while Fig. 2 is a photograph of the 16-channel system connected to a 16-coil flat spiral array (see Fig. 4) fitted with a 3D printed deformable skin (see Fig. 6).
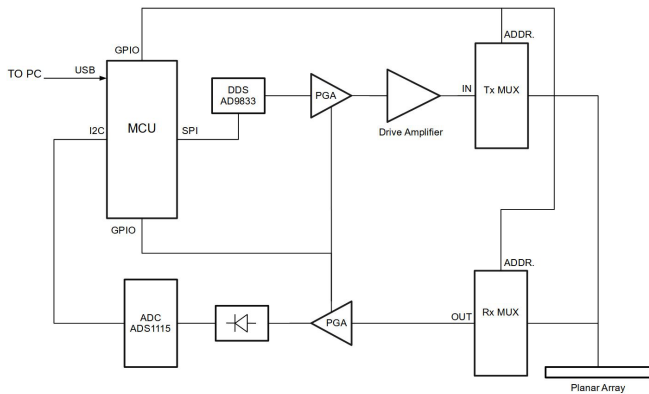

Fig. 1. Diagram of 8 and 16 channel MIT instruments, indicating the main system components.

Both 8-channel and 16-channel MIT devices can operate from between 1 kHz and 100 kHz. The 8-channel device operates at 10 frames/s and has an SNR of 83 dB for a frequency of 55 kHz, while the 16-channel has a speed of 1 frame/s and an SNR of 50 dB for circular coil and 53 dB for square coil array, both at 20 kHz. The self-inductance of the transmitting coil for the 8-channel system is approximately 180 μH, while the 16-channel accepts 250 μH coils. The inactive side of the coil array has partial shielding for protection against ambient interfering EM fields.

Fig 2: Photograph of 16-channel MIT instrument and 16-coil planar array with deformable membrane skin fitted, where a single membrane element of the skin is shown manually displaced or touched.

B.   Soft sensor design

An initial investigation used a coil array constructed from eight 40 mm diameter hand-wound coils, arranged as in Fig. 3.

Fig. 3: The 8-coil array sensor, indicating the coil distribution.

Each coil was measured using an LCR meter and found to have a self-inductance of 150 μH. Ideally, the sensor array would have been in a 3×3 configuration, however, this was limited by our 8-channel multiplexer. Therefore, a 'gap' existed where the 9th sensor would have otherwise been located.

The second sensor configuration is shown in Fig. 4, an array of 16 planar spiral coils arranged into a 4×4 array printed on a PCB. Each coil has an outer diameter of 70 mm, and an inner diameter of 30 mm and is composed of 51 turns, with a 5 mm spacing between neighboring coils. For the square coil array, the winding inner width is 25 mm and the outer width 75 mm; between two neighboring coils, there is a gap of 3 mm. The overall array dimensions are much greater than the initial 8-channel design (Fig. 3), having a total area of 900 mm^2, compared with the initial design of 256 mm^2, indicating the scalability of MIT sensors. The self-inductance of each planar coil was measured as 155 μH for circular coils and 157 μH for square coils, comparable with the coil inductance of the initial 8-channel array.

(a)   (b)

Fig. 4: (a) A 16-element array of circular coil sensors and (b) a 16-element array of square coil sensors.

For this EM-skin application a 'membrane' is required to approximate the dynamic response of human skin. The membrane initially used was a sponge substrate with a thin gauge copper sheet top-side lining. It was found that the deformation of the membrane was not localized, which coupled with poor recovery, leading to inconsistencies between the background data and the actual area of deformation. A different approach was then investigated, where a series of small cylindrical aluminum conductors are arranged into a 5×5 array, and the sponge substrate between them is cut to aid independent movement, so resulting in the alternative membrane skin as shown in Fig. 5.
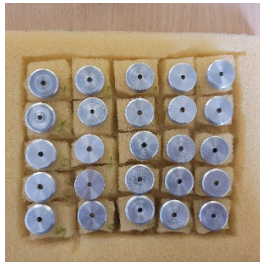

Fig. 5: A membrane skin using sponge and aluminum segments, forming a 5×5 array.

A further development was a novel 3D printed 8×8 spring array, where the conductor could be easily displaced vertically and recover to its original static positions, without disrupting any of the other conductor elements forming the membrane. The springs were designed using Autodesk Fusion 360, resulting in the skin structure as shown in Fig. 6. Each Spring had a height of 30 mm, a width of 22 mm, and an inter-spring separation of 13 mm. The springs were tapered to provide clearance when vertically displaced, so providing maximum range of movement.
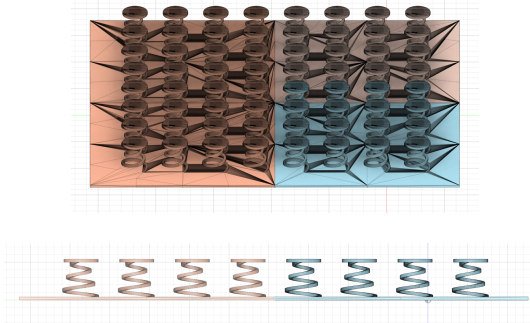

Fig. 6: A 3D printed deformable membrane.

C.   Image reconstruction

MIT utilizes an array of coils, arranged to define the region of interest, within which the electromagnetic property distribution is rendered as an image. The governing equation for the MIT forward model is given as equation (1), where μ is the permeability, ω the field angular frequency, and σ is the electrical conductivity. Here $\mathbf{B} = $ curl $\mathbf{A}$ where $\mathbf{A}$ is the magnetic vector potential, and $\mathbf{B}$ the magnetic flux density; $\mathbf{J_s}$ is the excitation current density, μ the permeability and j

the imaginary operator. In low-frequency excitation mode, the wave propagation effects can be ignored leading to an eddy current modeling problem, which is solved using an edge-based finite element model in 3D [12].

$$\nabla \times \frac{1}{\mu}\nabla \times \mathbf{A} + j\omega\sigma\mathbf{A} = \mathbf{J_s} \qquad (1)$$

The imaging principle is based on the laws of induction and eddy currents, which are induced by an AC magnetic field. The induced voltages in the receiving coils are calculated using volume integration over the receiving coil region, as equation (2), where $\mathbf{J_0}$ is a current density following in the strands of the receiving coil.

$$V_R = -j\omega \int A \cdot J_0 \, dv \qquad (2)$$

The V_R is the inducted voltage on receiver coil, given we use a constant current source in exciting coil represented by $\mathbf{J_s}$ the mutual inductance can be calculated between all pairs of coils. The mutual inductance will change when the metallic plates move up and down due to touch force.

The image reconstruction requires formulating the sensitivity distribution. The sensitivity distribution or so-called Jacobian matrix describes the relationship between the changes in induced voltage in receiving coils when there is a change in region $\boldsymbol{\Omega}$ with its electromagnetic properties. These changes are measured as a change in voltage, V_{mn}, induced by excitation coil m in a receiving coil n. The reciprocity theorem allows an efficient method of calculating these changes. If we assume that there is an excitation current I_m in coil m that produces electrical and magnetic fields E_m and B_m in region $\boldsymbol{\Omega}$, and the same process for when coil n acts as the excitation coil. The sensitivity can be efficiently calculated for changes in conductivity σ or permeability μ, as the dot product of those electric field $\mathbf{E}$ and magnetic field $\mathbf{B}$, which is already calculated in the forward model.

$$\frac{\partial V_{mn}}{\partial \sigma} = -\frac{j\omega}{I_m I_n} \int_\Omega E_m \cdot E_n \, d\mathbf{V} \qquad (3)$$

$$\frac{\partial V_{mn}}{\partial \mu} = -\frac{1}{I_m I_n} \int_\Omega B_m \cdot B_n \, d\mathbf{V} \qquad (4)$$

While the use of equations (3) or (4) links the induced voltage to the changes in electrical conductivity (or magnetic permeability), they need to be interpreted as a form of force, or touch. It is possible to use the MIT measurement device, with the direct definition of the partial derivative, to empirically create a Jacobian matrix that translates force (distance of the conducting membrane element) to the induced voltage. To create a measurement-based Jacobian matrix we used the membrane in Fig. 5 with the 8-channel MIT device. We collect a 28-point data frame (determined from $N(N-1)/2$, where N is the number of sensors), where all 25 membrane skin elements remain in their static positions (Fig. 5). This was used as reference data. Sequentially each conducting element of the membrane is vertically displaced, with the other 24 skin elements remaining in their static positions. In this way 25 × 28

matrix of measured data is created; subtracting this data from the reference data (all membrane elements in their static position, i.e., no force applied) enables the forming of a differential measurement-based Jacobian matrix. In imaging space, we can resize this 5×5-pixel sensitivity matrix, representing the 25 membrane elements (see Fig. 5) to a greater mesh-density. We used 46 × 46 pixels for 8-channel and 64 × 64 for 16-channel images. In the following section, both the force-based sensitivity map and the sensitivity map generated by equation (3) are used; generally, the performances are similar. For a low SNR measurement device, the measured sensitivity map may offer some benefits accounting for larger measurement uncertainties. In our devices with high SNR the two methods are identical.

The hypothesis is that interrogating the conducting membrane elements with different excitation frequencies results in changes in the measured induced voltage. The relationship between induced voltage and the internal material properties is nonlinear, which leads to a complicated nonlinear ill-posed inverse problem to be solved.   This is a challenging mathematical problem that is difficult to implement for real-time sensing. We linearized the relation between measured changes in boundary measurements ΔV as a function of changes in conductivity $\Delta\sigma$ or permeability $\Delta\mu$, which can be done through a Taylor expansion to produce:

$$\Delta V = J\Delta x \tag{5}$$

where J is the Jacobian which is essentially a set of 'sensitivity distributions' within the domain. The Tikhonov Regularization solves for Δx for changes in conductivity or permeabilities with the following equation:

$$\Delta x = (J^T J + \alpha^2 I^T I)^{-1} J^T \Delta V \tag{6}$$

where α is the regularization parameter, and I is the identity matrix. Other forms of regularization matrix such as NOSER regularization, Laplacian term, or a combination of them can be used. The number of pixels considered in J matrix (46 × 46 for 8 channels and 64 × 64 for 16 channels) is much higher than the number of independent measurements (28 for 8 channels and 120 for 16 channels). While this high pixel number allows the generation of the shape of touch and its morphology, the information gained is not higher than the number of measurements. The regularization term allows such a representation to be possible leading to a stable and well represented imaging outcome.

III. Multi-touchouch sensing

Experimental tests demonstrate the performance of the MIT sensor for touch detection. Both 8-channel and 16-channel devices were used in this study. Single touch, where a membrane element is independently displaced from its static position, was investigated using the 8-channel system with the array in Fig. 3, and the membrane structure shown in Fig. 5. Rendered images are shown in Fig 7a, where the location of applied pressure is apparent. Fig. 7b shows the images from the

displacement of two membrane elements simultaneously, indicating that two closely spaced locations are easily discernable. Extending to three simultaneous membrane element displacements in Fig. 7c, further indicates the practical rendering of multiple closely located inclusions. Inconsistencies in the pressure response (color values with multiple touch points) patterns result from the non-linear mechanical nature of the substrate sponge material. Fig 7d shows the results of membrane element displacement from the 16-channel system, again using the circular coil array in Fig. 4a and the membrane structure in Fig. 6. Single, double, triple, and quadruple touch points are shown, again indicating the ability to distinguish multiple element displacement. Given the larger number of coils and individual coil geometry, flat-spiral rather than cylindrical, the rendered images show greater resolution. Fig. 7e again shows multiple inclusions, as shown in Fig. 7d, but instead the square coil array in Fig. 4b was used. From Fig. 7e it is apparent that the rendered images show inclusions that are better defined, most likely resulting from the closer spacing of the square coils and hence greater magnetic coupling.

Appling different shaped solid objects to the skin membrane resulted in the rendered images shown in Fig. 8, where a long rectangular and a circular ring object are captured using the 8-channel arrangement.
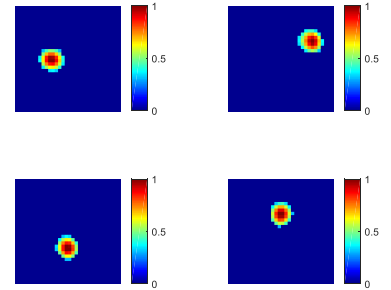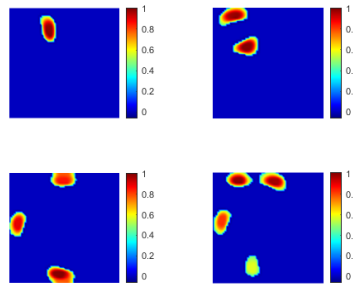

(a)   Single inclusion 8-channel system.
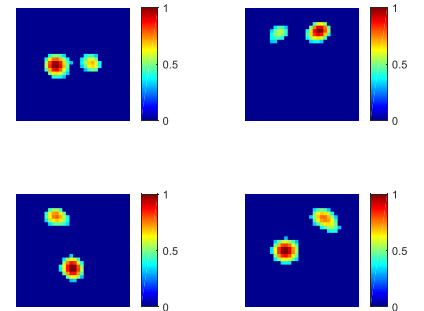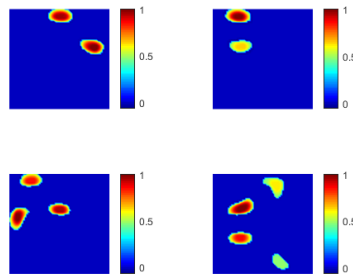

(b)   Double inclusions 8-channel system.
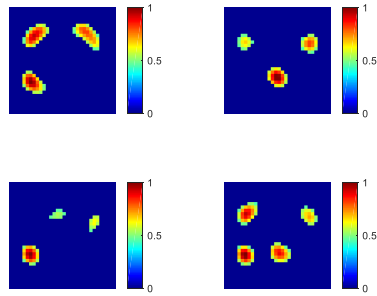
(c)   Three and four inclusions 8-channel system.

(d)   Multiple inclusions with a 16-channel system with the circular coil.

(e)   Multiple inclusions with a 16-channel system with the square coil.

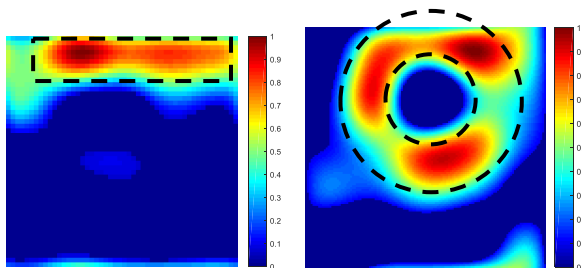**Fig. 7:** Single and multiple touch detection, scale normalized to maximum detected value.

Fig. 8: (a) A line shape and (b) a circular shape with 8 channels, scale normalized to maximum detected value.

Fig. 9 shows image stability, where a single membrane element is repeatedly displaced, and a dataset of 100 frames is then captured in the 8-channel device. Stacking the rendered images shows that there is little variation over the dataset, demonstrating the repeatability of the proposed skin. This very high position accuracy means that the ground truth location of touch points in Fig. 6 and the position reconstructed in Fig.7 are identical.
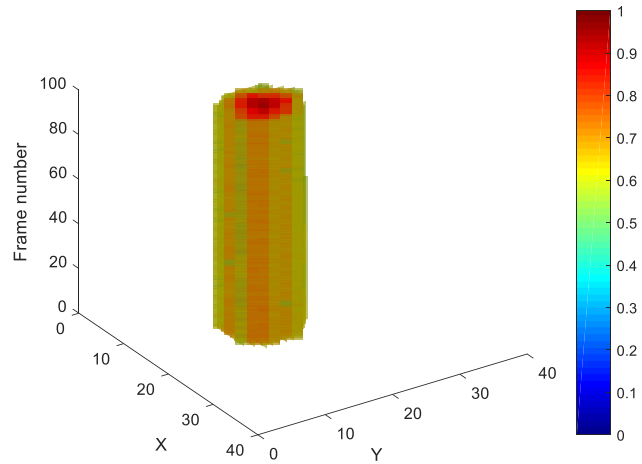
Fig. 9: Image stack from a repeated membrane element displacement (scale normalized to maximum detected value).

IV. DYNAMICAL SENSING

Given the high frame rate of the 8-channel system, it was possible to capture dynamic information, where frequency components present in the frame datasets reflected element motion. The manual cyclic displacement of a single membrane element at 3 Hz is shown in Fig. 10a, where the image stack indicates a periodic signature. Taking the mean value of each frame in the dataset gives a time domain signal, also shown in Fig. 10b, where this cyclic nature is also evident. Taking the Fourier transform of the frame mean results in a spectrum, where the 3 Hz component is seen in Fig. 10c. Similarly, Fig. 11 shows the effect of simultaneous multiple manual cyclic membrane element displacements at different frequencies, 0.5 Hz and 2 Hz, arbitrarily chosen to be within the frame rate capability of the instrument and membrane dynamics, such as mechanical hysteresis. From the image stack, rendered from the captured frame dataset, the two membrane elements indicate the different cyclic displacement frequencies, where two individual membrane elements were actuated simultaneously. Taking the mean for each frame results in a complicated time domain signal, however the spectrum clearly shows the two frequency components from the two membrane elements. Other frequency components are also present in the spectrum, which are the result of complicated membrane element motion and membrane substrate dynamics. But the more significant stimulation of 2 Hz and 0.5 Hz are observable in the frequency analysis of dynamical imaging data. Figs 10a and 11a are scaled to

the maximum detected value, while Fig. 10b, 10c, 11b and 11c y-axis scale are derived from the raw measured values.

Fig. 10: Single membrane element displacement at a frequency of 3 Hz, (a) stack of 2D images, scale normalized to maximum detected value, (b)time or frame number domain mean value of measured   data, (c) frequency analyses of part (b) data.
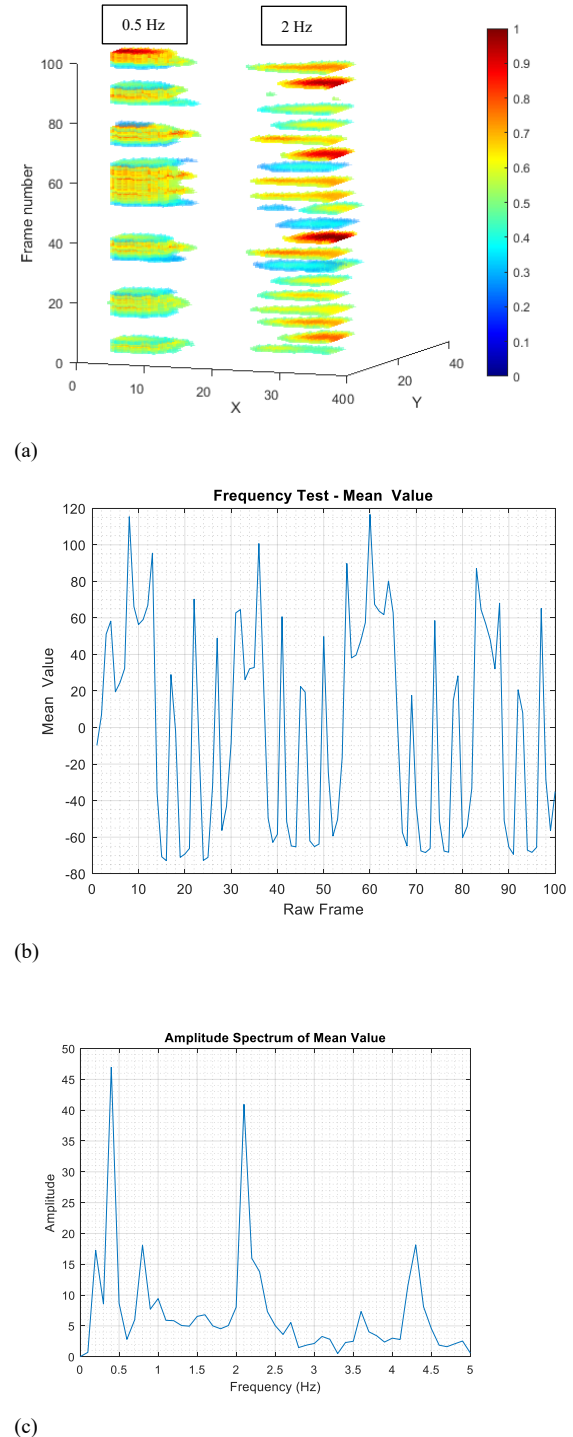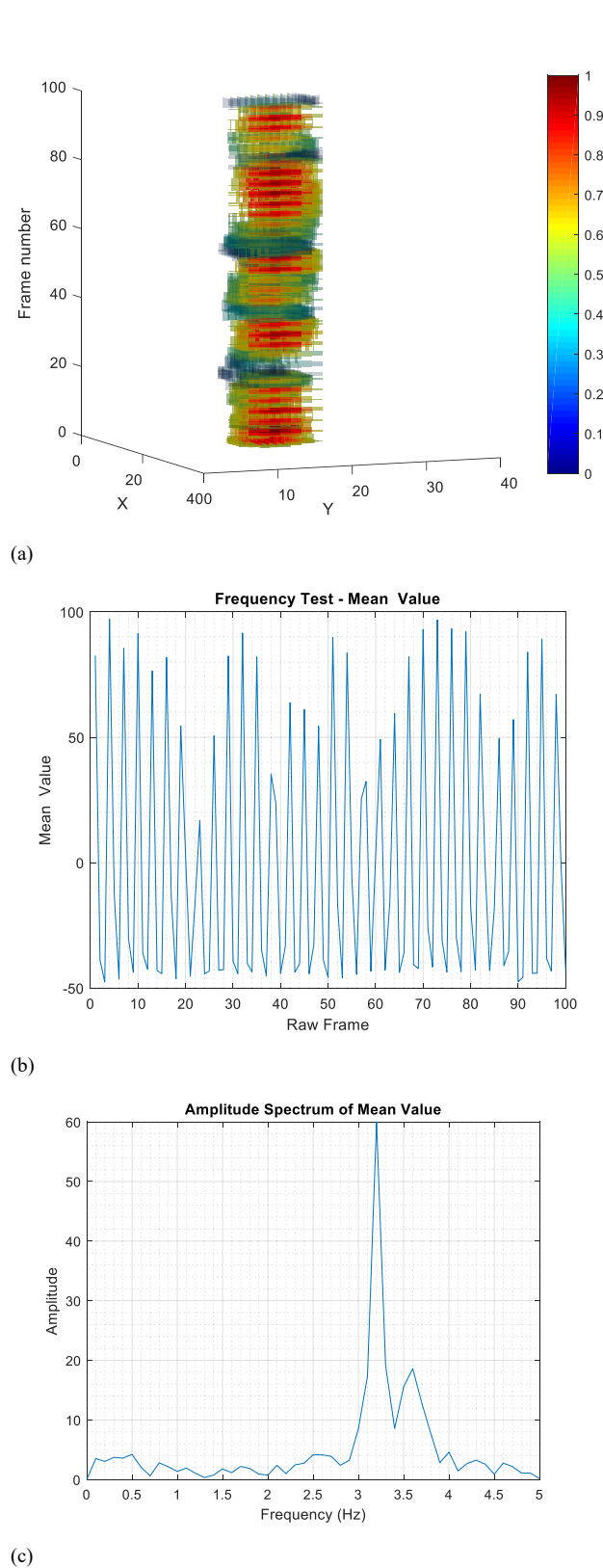

(a)



(b)

(c)

(a)

(b)

(c)

Fig. 11: Simultaneous cyclic membrane element displacements with frequencies 2 Hz and 0.5 Hz (a) stack of 2D images, generated by simultaneous actuation of two individual membrane elements at the two different frequencies, (b) time or frame number domain mean value of measured data, (c) frequency analysis of data shown in (b).
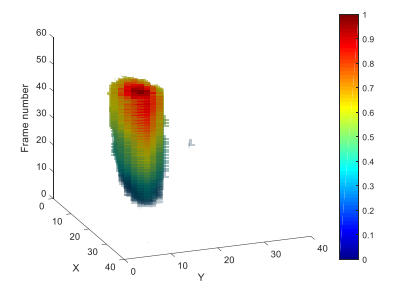
V. QUANTITATIVE IMAGING

In determining the ability of the membrane to detect the location and dynamic frequency of applied forces, only bistatic displacement is considered, that is, the element is either in the rest static position, or displaced proximal to the coil array. Figs. 12, 13 and 14 show the force quantification.
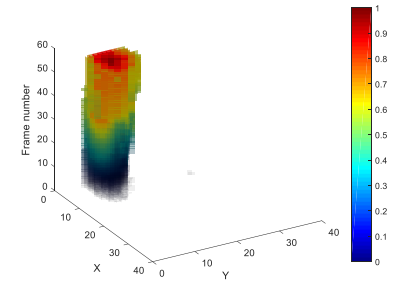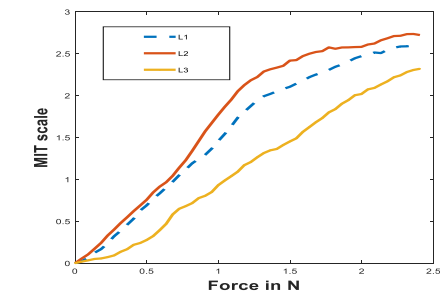

(a)
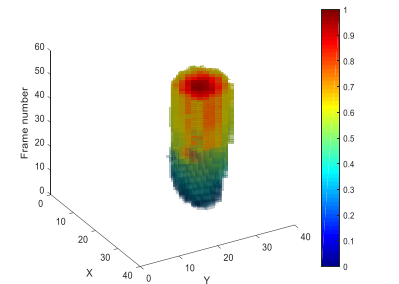
(b)

(c)

(d)

Fig. 12: Force applied to three locations in 8-channel MIT device, (a), (b), (c) the stack of frame images with increasing forces, (d) MIT image mean vs actual force applied.
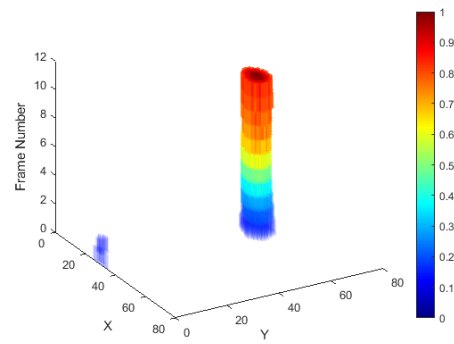
(a)

(b)

(c)

(d)

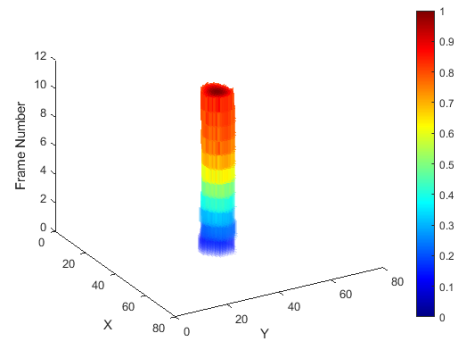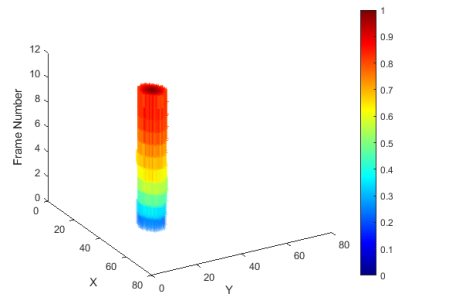**Fig. 13:** Force applied to three locations in a 16-channel MIT device. (a), (b), (c) the stack of frame images with increasing forces, (d) MIT image mean vs actual force applied.

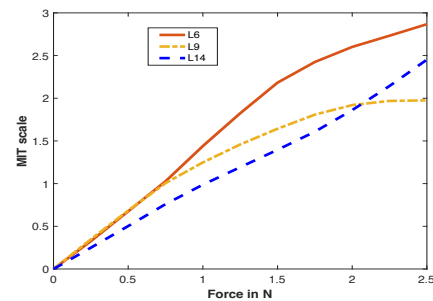Linear vertical motion of the element translates to a measure of applied force, based on the membrane substrate dynamics, resulting in useful quantitative data. Both the 16 and 8-channel systems were investigated, where a linearly increasing force

was applied to different elements of the membrane, achieved by linearly increasing the water content of a suitably sized container. With each increment of the water level frame data was collected and an image rendered. Image stacks for three different locations are shown for the 8-channel system in Fig. 12, while Fig. 13 shows the response for the 16-channel instrument. The force applied to various locations is shown as L1, L2, and L3 in 8 channel system and L6, L9, and L14 in 16 channel system. The actual positions in the X-Y plane are shown in Fig. 12 and 13, the entire skin areas have 46×46 pixels in 8 channels and 64×64 pixels in 16 channels as stated earlier. Figs. 12a-c and 13a-c use a scale normalized to the maximum detected value. Also shown are the calibration plots for the three different locations, indicating the image mean value in that region as a function of real applied force. The real applied force is based on the steps of weights added during these experiments. There is a clear correlation between the MIT image value and force, which has some dependence upon the location of force applied to the membrane skin. The MIT image vs. force plot shows the expected saturation or decrease in gradient. The force-based experiments were carried out using both the 8-channel and 16-channel devices, where the circular coil array fitted with the sponge-based membrane shown in Fig. 5, formed the EM skin. As more weight is added, the membrane substrate between the skin conducting element and the coil sensor compresses, eventually more force is needed for further compression, resulting in the saturation region of the plot.

Quantitative data analysis allows for force calibration by collecting measurements at various locations. Fig. 14 shows the calibration curve for the force analysis at the position of L6 from Fig. 13. As it can be seen, a quadratic equation can produce a suitably good fitting function, showing high correlation with actual measurement. In future studies, in addition to the eddy current models used here a mechanical modelling tool can help evaluate the expected forces vs MIT scaling values by accounting for the elastic properties of the interface membrane.
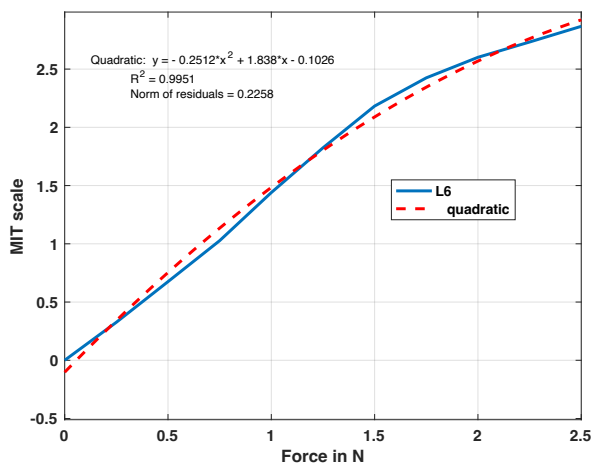

Fig. 14: Force calibration using a quadratic data fitting

From the relaxed static position of the membrane element, the force-distance gradient is detectable by the MIT sensor array. Although the minimal detectable force has some dependency

on the applied force location, skin membrane substrate, and the coil array, a 120 mN force, applied using known weights, is detectable if applied to one of the conductive membrane elements. With the membrane element diameter of 1 cm, this force of 120 mN translates to a pressure of around 0.38 kPa.

V. DISCUSSIONS AND CONTEXT

There are growing research activities to create large areas of tactile sensing [14]. Capacitive [15], and inductive [13] types of transducers have been used in matrix form sensors allowing for scalability and reliability of large-scale skin. Tomographic-based methods have also been used as part of efforts in developing a sense of touch in robotics. EIT-based sensors are the most widely used tomographic skin sensors [1]. There are benefits to tomographic-based skin including more measurement data, and more automated data processing. In this paper, we have extended the inductive proximity sensing to a fully functional inductive tomographic touch and force sensor. While the MIT device is sophisticated, the membrane and mechanical interaction are simplified. Future studies could include validation and modelling of elastomeric membrane as well as the MIT measurement and imaging. This will allow a full uncertainty quantification and performances analysis. A future study could further investigate the geometrical flexibility as well as challenges related to the deployment of such an imaging sensor in robotics [17] or other intelligent platforms. This is the first demonstration of MIT imaging for tactile applications that will open significant new opportunities for further developments.

VI. CONCLUSION

The paper introduces a novel artificial robotic skin using mutual induction tomography. The experimental results show a reliable, robust, and secure artificial skin sensor using MIT imaging. The evaluation test results were conducted indicating the performance of the new sensor in terms of both magnitude and location of single and multiple points of contact, as well as the dynamic and quantitative characteristics of applied force. Tomographic-based skin for touch sensing is an attractive method amongst methods used in the development of biomimetic skins for soft robots. This likely requires the development of multimodal sensing capabilities in flexible, stretchable, and healable materials and systems. This paper demonstrates such a functionality using MIT, which provides continuum sensing with few coils, but still with high resolution, large area, and remote sensor positioning, so as not to interfere with robotic physical interactions. This suggests that MIT could then become an important component in future tomographic-based skin sensor systems. Our continued studies will focus on how the MIT-based sensor can be employed in multimodality sensing membranes, as well as furthering capabilities of the MIT-based skin by establishing further uncertainty quantification.

REFERENCES

[1] K. Park, H. Yuk, M. Yang, J. Cho, H. Lee, and J. Kim. "A biomimetic elastomeric robot skin using electrical impedance and acoustic tomography for tactile sensing." *Science Robotics* 7, no. 67: eabm7187, 2022.

[2] M. Watanabe et al., "Impact of intraoperative adjustment method for increased flexion gap on knee kinematics after posterior cruciate ligament-sacrificing total knee arthroplasty," Clin. Biomech., vol. 63, pp. 85–94, Mar. 2019.

[3] R. Karpi´nski, Ł. Jaworski, J. Jonak, and P. Krakowski, "Stress distribution in the knee joint about tibiofemoral angle using the finite element method," in Proc. MATEC Web Conf., Kazimierz Dolny, vol. 252, 2019, p. 07007.

[4] J. Ji, Y. Qi, J. Liu, and K.-M. Lee, "Reconfigurable impedance sensing system for early rehabilitation following stroke recovery," in Proc. IEEE/ASME Int. Conf. Adv. Intell. Mechatronics (AIM), Boston, MA, USA, Jul. 2020, pp. 1131–1136.

[5] F. Lin, A. Wang, Y. Zhuang, M. R. Tomita, and W. Xu, "Smart insole: A wearable sensor device for unobtrusive gait monitoring in daily life," IEEE Trans. Ind. Informat., vol. 12, no. 6, pp. 2281–2291, Dec. 2016.

[6] T. Hellebrekers, N. Chang, K. Chin, M. J. Ford, O. Kroemer, and C. Majidi, "Soft magnetic tactile skin for continuous force and location estimation using neural networks," IEEE Robot. Autom. Lett., vol. 5, no. 3, pp. 3892–3898, Jul. 2020.

[7] M. L. Preti, M. Totaro, E. Falotico, M. Crepaldi, and L. Beccai, "Online Pressure Map Reconstruction in a Multitouch Soft Optical Waveguide Skin. " *IEEE/ASME Transactions on Mechatronics, 2022.*

[8] J. Li, K.M. Lee, "A Novel Method for Soft Contact Sensing Based on Electrical Impedance Sensitivity Images" *IEEE Sensors Journal*, *22*(10), 9296-9305, 2022.

[9] G. Ma, & M. Soleimani, "A versatile 4D capacitive imaging array: a touchless skin and an obstacle-avoidance sensor for robotic applications. " *Scientific Reports*, *10*(1), 1-9, 2020

[10] H. Yuan, T. Lei, Y. Qin, R. Yang. "Flexible electronic skins based on piezoelectric nanogenerators and piezotronics. ", *Nano Energy*, *59*, 84-90, 2019.

[11] L. Ma, M. Soleimani, . "Magnetic induction tomography methods and applications: A review. " *Measurement Science and Technology*, *28*(7), 072001. 2017.

[12] M. Soleimani, W.R.B. Lionheart, A. J. Peyton, X. Ma, S.R. Higson. "A three-dimensional inverse finite-element method applied to experimental eddy-current imaging data". *IEEE Transactions on Magnetics*, *42*(5), 1560-1567, 2006.

[13] L. Wang, D. Jones, G. .J Chapman, H. J. Siddle, D. A. Russell, A. Alazmani, and P. Culmer, "An Inductive Force Sensor for In-Shoe Plantar Normal and Shear Load Measurement. " IEEE Sensors Journal, 20 (22). pp. 13318-13331, 2020

[14] A Schmitz, P Maiolino, M Maggiali, L Natale, G Cannata, G Metta, "Methods and technologies for the implementation of large-scale robot tactile sensors, " IEEE Transactions on Robotics 27 (3), 389-400.

[15] P Maiolino, M Maggiali, G Cannata, G Metta, L Natale, "A flexible and robust large scale capacitive tactile system for robots, " IEEE Sensors Journal 13 (10), 3910-3917.

[16] G. Li, S. Liu, L. Wang, "Skin-inspired quadruple tactile sensors integrated on a robot hand enable object recognition. " *Sci. Robot.* **5**, abc8134 (2021).

[17] R. S. Dahiya, G. Metta, M. Valle, G. Sandini, "Tactile sensing—From humans to humanoids." IEEE Trans. Robot. 26, 10.1109/TRO.2009.2033627 (2010).

GAVIN DINGLEY received a B.Eng. degree in electrical engineering from Cranfield University, RMCS, Shrivenham in 2003 and has researched in areas including radar, electromagnetic materials, antennas, and medical ultrasonics. Presently employed by the Department of Electronic and Electrical Engineering, University of Bath, UK, as an experimental officer, specializing in RF electronics. Also, a PhD candidate for magnetic induction tomography within the Engineering Tomography Laboratory (ETL), University of Bath.

MACKENZIE COX began a MEng degree in Electronic and Electrical Engineering in 2018 at the University of Bath. In 2020-21, he joined Semtech LTD for an industrial placement role as part of the Test Engineering team. Later, in 2022 he took up a Research Assistant role with Manuchehr Soleimani in the Engineering Tomography Laboratory (ELT), University of Bath, working on various areas of tomographic imaging.

MANUCHEHR SOLEIMANI received a B.Sc. degree in electrical engineering, an M.Sc. degree in biomedical engineering, in 1996 and 1999 from Sharif University of Technology Iran and a Ph.D. degree in inverse problems and electromagnetic tomography from The University of Manchester, Manchester, U.K., in 2005. From 2005 to 2007, he was a Research Associate with the School of Materials, The University of Manchester. In 2007, he joined the Department of Electronic and Electrical Engineering, University of Bath, Bath, U.K., where he was a Research Associate and became a Lecturer in 2008, a Senior Lecturer in 2013, a Reader in 2015, and a Full Professor, in 2016. In 2011, he founded the Engineering Tomography Laboratory (ETL), University of Bath, working on various areas of tomographic imaging, in particular multi-modality tomographic imaging. He has authored or co-authored 350 publications in the field of tomographic imaging.